nature materials

Article

https://doi.org/10.1038/s41563-025-02254-2

Symmetry-protected electronic metastability in an optically driven cuprate ladder

Received: 5 November 2024

Accepted: 1 May 2025

Published online: 03 June 2025

Check for updates

Hari Padma[1] ✉, Filippo Glerean[1], Sophia F. R. TenHuisen[1,2], Zecheng Shen[3], Haoxin Wang[4], Luogen Xu[3], Joshua D. Elliott[5], Christopher C. Homes[6], Elizabeth Skoropata[7], Hiroki Ueda[7], Biaolong Liu[7], Eugenio Paris[7], Arnau Romaguera[7], Byungjune Lee[8,9], Wei He[10], Yu Wang[11,12], Seng Huat Lee[11,12], Hyeongi Choi[13], Sang-Youn Park[13], Zhiqiang Mao[11,12], Matteo Calandra[14], Hoyoung Jang[13], Elia Razzoli[7], Mark P. M. Dean[10], Yao Wang[3] ✉ & Matteo Mitrano[1] ✉

Optically excited quantum materials exhibit non-equilibrium states with remarkable emergent properties, but these phenomena are usually transient, decaying on picosecond timescales and limiting practical applications. Advancing the design and control of non-equilibrium phases requires the development of targeted strategies to achieve long-lived, metastable phases. Here we report the discovery of symmetry-protected electronic metastability in the model cuprate ladder $Sr_{14}Cu_{24}O_{41}$. Using femtosecond resonant X-ray scattering and spectroscopy, we show that this metastability is driven by a transfer of holes from chain-like charge reservoirs into the ladders. This ultrafast charge redistribution arises from the optical dressing and activation of a hopping pathway that is forbidden by symmetry at equilibrium. Relaxation back to the ground state is, hence, suppressed after the pump coherence dissipates. Our findings highlight how dressing materials with electromagnetic fields can dynamically activate terms in the electronic Hamiltonian, and provide a rational design strategy for non-equilibrium phases of matter.

Ultrafast laser pulses have advanced the frontier of quantum materials research, enabling the creation of dynamical states with emergent properties and functionalities[1]. Strong optical fields can hybridize with solids or selectively excite their microscopic degrees of freedom, leading to remarkable phenomena such as photoinduced topological[2,3], magnetic[4,5] and superconducting[6,7] phases. However, the transient nature of these phenomena—often limited to the duration of the optical field or decaying shortly thereafter—prevents their use in functional applications.

Sometimes, dynamical responses result in metastable or 'hidden' phases of matter. These long-lived states are rare and form due to dynamical bottlenecks in their relaxation back to equilibrium. Photoexcited materials can become trapped in an intermediate state due to energy barriers created by structural effects, phase separation, and domain nucleation and growth processes[8–18]. Metastable states can also emerge due to topologically protected defects[19,20], glassy behaviour[21] or trapping by impurities[22]. These mechanisms rely on an interplay of structural and electronic degrees of freedom and are unique to the physics of each material. Progress in the creation and control of metastable non-equilibrium phases, however, requires the formulation of more general design principles.

A full list of affiliations appears at the end of the paper. ✉e-mail: hpadmanabhan@g.harvard.edu; yao.wang@emory.edu; mmitrano@g.harvard.edu

https://doi.org/10.1038/s41563-025-02254-2

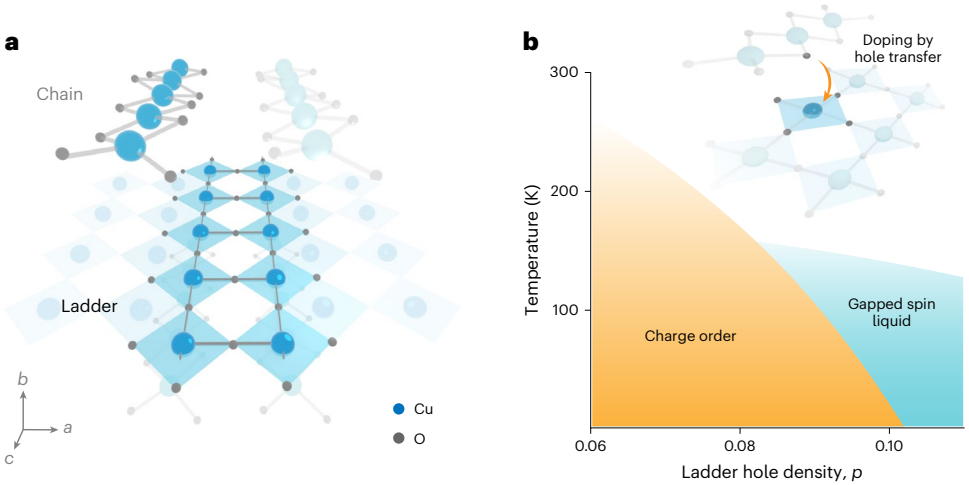

Fig. 1 | Structure and electronic phases of $Sr_{14}Cu_{24}O_{41}$. a, This quasi-one-dimensional compound consists of alternating ladder and chain layers with an incommensurate periodicity along the *c* axis. The chains comprise edge-sharing CuO_4 squares, whereas the ladders feature corner-sharing CuO_4 plaquettes. Neighbouring ladders are shifted by half a period along the *c* axis. Intercalating Sr atoms are omitted for clarity. **b**, Schematic of the phase diagram[32] of $Sr_{14}Cu_{24}O_{41}$. This compound is naturally self-doped, with most holes localized in the chains and a residual hole density of $p = 0.06$ in the ladders. Isovalent Ca substitution at the Sr sites transfers holes from the chains to the ladders, increasing the ladder hole density. On doping, the ladders transition from a charge-ordered phase to a gapped spin liquid phase.

A possible strategy for achieving metastability in a broad range of quantum materials is to optically engineer their underlying Hamiltonian. This approach leverages the coherent optical dressing of electronic states by an incident electromagnetic field, a technique recently used to manipulate band structures[2,3], break electronic symmetries[23] and modulate nonlinear optical properties[24] in various solids. Although optical dressing is by itself transient, occurring only in the presence of the driving field, it can renormalize electronic interactions and act as a gate to induce lasting changes in the electronic distribution of a material[25]. This raises the possibility of temporarily switching specific terms in the Hamiltonian and driving the system into a metastable excited state.

Although this approach may be broadly applicable, one-dimensional strongly correlated materials are particularly suited to test it due to their inherent tendency towards metastability. First, electronic relaxation in these systems is constrained by dimensionality, as charge motion is restricted to one direction. Second, partial or complete spin–charge separation suppresses the decay of non-equilibrium electronic distributions via spin fluctuations[26]. Third, many-body interactions further slow relaxation by increasing the energy cost of scattering processes[27] and creating symmetry-protected dark states[28]. These features open the door to the realization of previously unobserved metastable or hidden states driven by purely electronic mechanisms.

Here we observe electronic metastability in the quasi-one-dimensional cuprate ladder $Sr_{14}Cu_{24}O_{41}$. We optically induce a non-equilibrium metastable state that persists for at least tens of nanoseconds. Time-resolved terahertz (THz) reflectivity measurements, combined with ultrafast resonant X-ray scattering and spectroscopy, reveal that this metastable state involves hole transfer from chain-like charge reservoirs into the ladders. At equilibrium, symmetry constraints suppress hopping between the two structural subunits, effectively decoupling them. The pump laser optically dresses the Zhang–Rice singlet states and transiently breaks their symmetry, thereby enabling hole tunnelling between chains and ladders. Once the external field is removed, the symmetry is restored, trapping the holes in their new configuration. Our findings demonstrate electronic metastability through transient Hamiltonian engineering and define a general approach to realize long-lived non-equilibrium states.

Optically induced metastability

$Sr_{14}Cu_{24}O_{41}$ is an intrinsically self-doped charge transfer insulator with one hole for every four Cu ions. Its unit cell comprises alternating layers of incommensurate chain-like and ladder-like subunits (Fig. 1a). The chains act as hole-rich charge reservoirs[29,30], whereas the ladders host the remaining holes that propagate in a spin-singlet background. Below $T_{CO} = 250$ K, these carriers self-organize into a long-range charge-ordered phase[31]. In particular, isovalent Ca substitution induces hole transfer from the chains to the ladders (Fig. 1b), increasing the ladder hole density. This doping results in a suppression of charge order and a transition into a gapped spin liquid phase[32]. At higher hole densities, a superconducting phase is stabilized under moderate external pressures[32,33].

In our experiments, we use intense near-infrared pulses to drive $Sr_{14}Cu_{24}O_{41}$ single crystals (Methods provide details about the sample characterization). Pump pulses, tuned just below the charge transfer gap energy (1.55 eV, 35-fs pulse duration), are polarized along the *c* axis to excite Cu–O transitions along the ladder legs with peak fields up to 7.7 MV cm^{-1}. We track the pump-induced changes in the low-energy optical properties using delayed quasi-single-cycle THz pulses reflected from the photoexcited samples (Fig. 2a, Methods and Supplementary Section 1). On exciting the sample in the charge-ordered phase (100 K), we observe a reflectivity enhancement with a sub-picosecond rise time, consistent with previous reports[34], which unexpectedly persists for several nanoseconds (Fig. 2b). This long-lived state is non-thermal, as indicated by the transient reflectivity and optical conductivity $\sigma_1(\omega)$ (Fig. 2c,d). In particular, the transient σ_1 suggests a reduction in the charge gap, in contrast to the gap filling that is observed across the temperature-dependent charge order transition at equilibrium (Supplementary Fig. 1e). These spectral changes resemble the effects of doping holes into the ladder through Ca substitution, which gradually suppresses the charge-ordered phase by closing its gap[35] (Supplementary Section 1 and Supplementary Fig. 2). This points to a metastable enhancement in hole density in the ladders.

X-ray evidence of metastable hole transfer

To determine the microscopic character of the observed metastability, we interrogate the photoexcited state with a combination of ultrafast resonant X-ray techniques, each addressing a distinct observable. We first examine the non-equilibrium charge order modulation with

https://doi.org/10.1038/s41563-025-02254-2

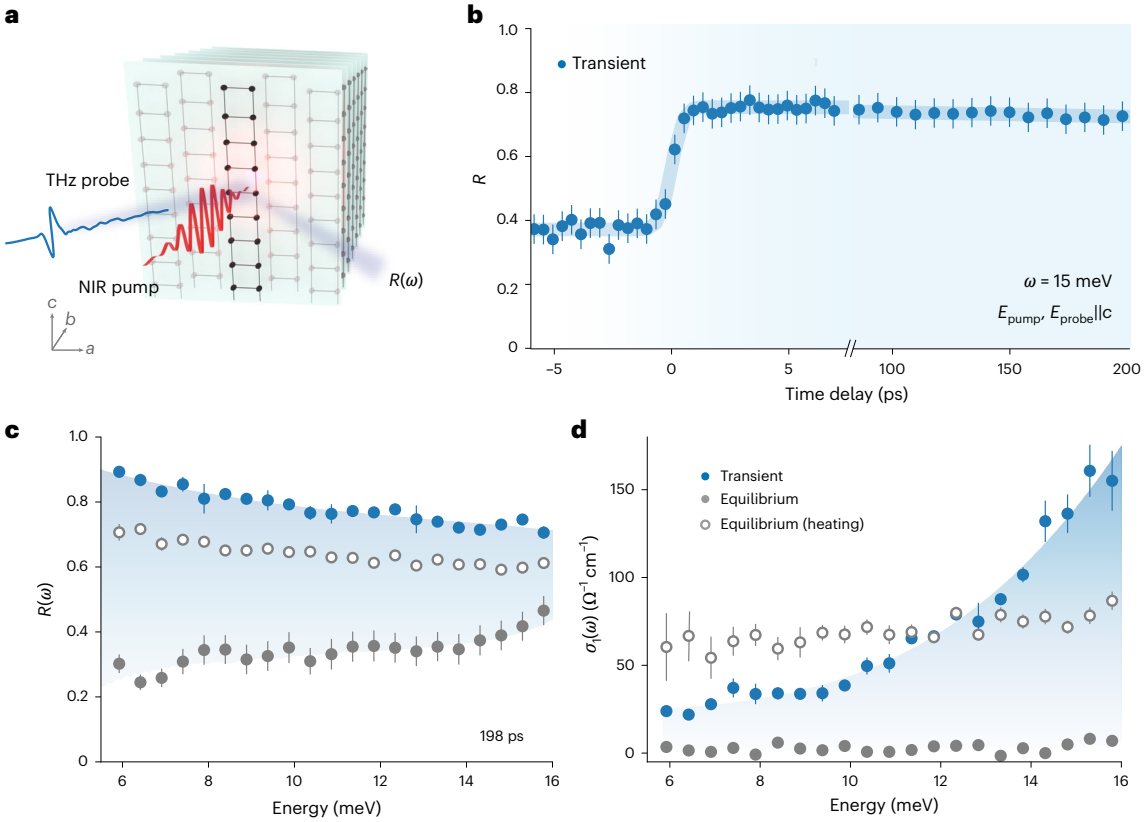

Fig. 2 | Observation of light-induced metastability. a, Sketch of a pump–probe experiment on the cuprate ladder $Sr_{14}Cu_{24}O_{41}$, with near-infrared (NIR) pump (photon energy, 1.55 eV; electric field, 7.7 MV cm^{-1}) and THz probe pulses in the reflection geometry. **b**, Time-dependent reflectivity $R(\omega)$ along the *c* direction at a representative energy (blue symbols), featuring a sharp increase and a transition into a metastable electronic state. The blue line is a fit to the data. **c**,**d**, Reflectivity $R(\omega)$ (**c**) and optical conductivity $\sigma_1(\omega)$ (**d**) of the metastable state (t = 198 ps). Non-equilibrium optical properties (blue circles) are measured at 100 K. Equilibrium data are measured at 100 K (grey circles) and 250 K (open grey circles, labelled 'heating'). Data are presented as mean values, and the error bars are the standard deviation of 114 independent scans. The blue-shaded areas highlight photoinduced spectral changes.

resonant X-ray diffraction at the O K edge (Fig. 3a). Below T_{CO} = 250 K, ladder holes form a commensurate density wave with periodicity $5c_L$ (c_L, lattice parameter of ladder plaquettes) without detectable structural distortions[31]. At resonance with the mobile holes, we observe an intense Bragg peak corresponding to the charge modulation at q_{CO} = (0, 0, 0.2) reciprocal lattice units (r.l.u.) (Fig. 3b and Supplementary Section 2). On pumping along the ladder rungs, we observe a sudden reduction in diffraction intensity, consistent with a partial suppression of the charge-ordered phase. This suppression persists unchanged up to 1 ns (Fig. 3c), indicating a long-lived photoexcited state with a lifetime exceeding tens of nanoseconds at all the measured fluences (Supplementary Fig. 4). This behaviour contrasts sharply with that of two-dimensional cuprates, where partially suppressed charge order recovers within picoseconds[36]. Moreover, the absence of peak broadening is incompatible with pump-induced disordering, contrary to melting-involving topological defects[20,36]. In particular, the charge order suppression occurs exclusively on pumping within the ladder plane (Fig. 3c). This rules out an out-of-plane ladder-chain dipole excitation as a dominant mechanism for the observed response. The charge order suppression closely correlates with the long-lived changes in the optical properties, confirming that the charge order correlations are weaker in the non-equilibrium state.

Next, we present a direct measurement of the valence hole distribution with time-resolved X-ray absorption spectroscopy (trXAS), which constitutes the key observation of this work. We tune the X-rays at resonance with the Cu L_3 edge, where the absorption spectrum features two peaks reflecting the different local bonding of Cu atoms[37] (Fig. 4a). The peaks at 932.5 eV and 934.4 eV each feature contributions primarily from the corner-sharing ladders and edge-sharing chains, respectively (Fig. 4b, Supplementary Section 3 and Supplementary Figs. 5–7). At equilibrium, the Cu L_3-edge X-ray absorption (XAS) spectrum is sensitive to changes in the hole distribution and undergoes a reshaping due to chain-to-ladder hole transfer induced by isoelectronic Ca substitution[30,37] (Supplementary Section 3 and Supplementary Fig. 5). The trXAS spectrum of the metastable state simultaneously shows a suppression of the chain peak and an enhancement at the shoulders of the ladder resonance (Fig. 4c). The differential non-equilibrium response (Fig. 4c) may be compared with the effect of Ca substitution at equilibrium (Fig. 4d) corresponding to a chain-to-ladder hole transfer of Δp = 0.06 holes per Cu_L (ref. 30; Cu_L, Cu atoms on the ladder). The differential XAS changes are remarkably similar and indicate a pump-induced hole transfer from the chain reservoirs to the ladders (Fig. 4e). Since the amplitude of the spectral reshaping scales linearly with the transferred hole density[37] (Supplementary Section 3 and Supplementary Fig. 6), we can quantify a non-equilibrium chain-to-ladder hole transfer of Δp = 0.03 holes per Cu_L. The chain-to-ladder hole transfer is further corroborated by our trXAS measurements at the O K edge (Supplementary Section 4 and Supplementary Figs. 9 and 10). Finally, the time-delay dependence of the trXAS spectra (Supplementary Fig. 8a) confirms that after an initial fast relaxation, the hole transfer is long-lived, mirroring the optical gap closure and charge order suppression.

Impurities are known to influence the carrier and spin dynamics in cuprates, sometimes resulting in localization[38,39]. Such effects could localize holes in the ladders and prevent them from returning to the chains, potentially giving rise to metastability. To determine whether

https://doi.org/10.1038/s41563-025-02254-2

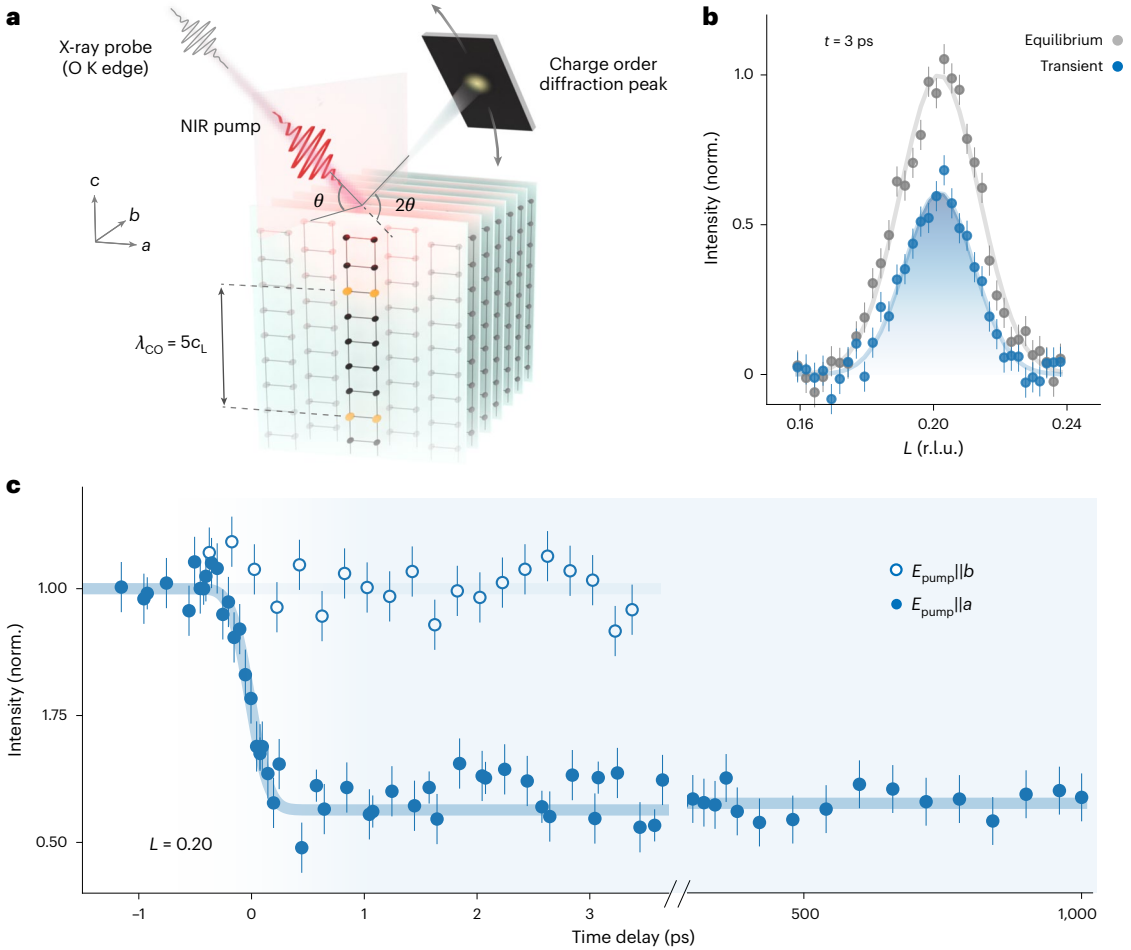

Fig. 3 | Metastable charge order suppression. a, Sketch of the trXRD experiment, with X-ray probe pulses resonant with the O K edge ($\hbar\omega$ = 528.6 eV). The charge-ordered phase with $\lambda_{CO} = 5c_L$ is shown schematically. **b**, Equilibrium (light grey) and transient (blue) charge order diffraction peak of the ladder. **c**, Light-induced charge order suppression is metastable up to nanosecond timescales. Data are presented as mean values, and the error bars are the standard deviation of 11 data points at negative time delays. The shaded regions indicate the onset of electronic metastability. There is no peak suppression when the pump is polarized normal to the ladder plane ($E_{pump}||b$).

the transferred holes in the ladders exhibit localized or itinerant character, we leverage the sensitivity of magnetic excitations to the doped carriers. We measure the magnetic excitation spectrum of the ladders with time-resolved resonant inelastic X-ray scattering (trRIXS) at the Cu L_3 edge (Fig. 5a). Undoped ladders with isotropic couplings naturally form spin singlets[40]. These give rise to dispersive singlet-to-triplet transitions ('triplons') as elementary magnetic excitations (Supplementary Section 5 and Supplementary Fig. 11), which appear as a two-triplon continuum at our measured wavevectors. In Fig. 5b, we present the equilibrium dynamical spin structure factor $S(q, \omega)$ extracted from our resonant inelastic X-ray scattering (RIXS) data and calculated via density matrix renormalization group (DMRG; Methods, Supplementary Section 5 and Supplementary Figs. 12–15 provide more details). The experimental intensity map reveals a well-defined two-triplon continuum with positive dispersion, consistent with previous studies[41].

The introduction of holes results in distinct changes to the two-triplon continuum, dependent on whether the holes are itinerant or localized (Fig. 5c). Itinerant holes are expected to marginally suppress and broaden the triplon continuum as they disrupt the singlet background[42]. By contrast, localized holes additionally localize the neighbouring triplons, which would cause striking, qualitative changes to the dispersion[39]. On photoexcitation into the metastable state, we observe a suppression of the two-triplon continuum, particularly near L = 0.25 r.l.u. (Fig. 5d). Within the limits of our experimental resolution, we detect no changes to the shape of the two-triplon dispersion. The differential trRIXS intensity is quantitatively reproduced in our DMRG calculations by incorporating an additional 0.03 holes per Cu_L with an itinerant character. By contrast, the calculated differential intensity for localized holes (Supplementary Section 6) shows a suppression near L = 0.25 r.l.u. that is three times greater than that observed in the experimental spectra, accompanied by enhanced intensity at lower energy loss. These results indicate the itinerant nature of the ladder holes and argue against hole localization as the cause of the observed metastability.

Optical activation of a symmetry-forbidden hopping

Finally, we turn to the microscopic origin of the metastable state. We first note that the ladder and chain subunits are effectively decoupled at equilibrium. The primary route for tunnelling between the two subunits would be via the O atoms in the chain that are closest to the CuO_4 plaquettes in the ladder. These approximately 'apical' chain O atoms, identified by prior diffraction studies[43,44], form weak bonds with the ladder plaquettes every 3–5 ladder unit cells. At equilibrium, the direct hopping t_{ap} along this pathway is vanishingly small, resulting in an effective decoupling of holes in the chains and ladders (Fig. 6a). This is a consequence of the ladder holes forming Zhang–Rice singlet states composed of Cu $3d_{x^2-y^2}$ and surrounding O $2p_{x/y}$ orbitals on each

https://doi.org/10.1038/s41563-025-02254-2

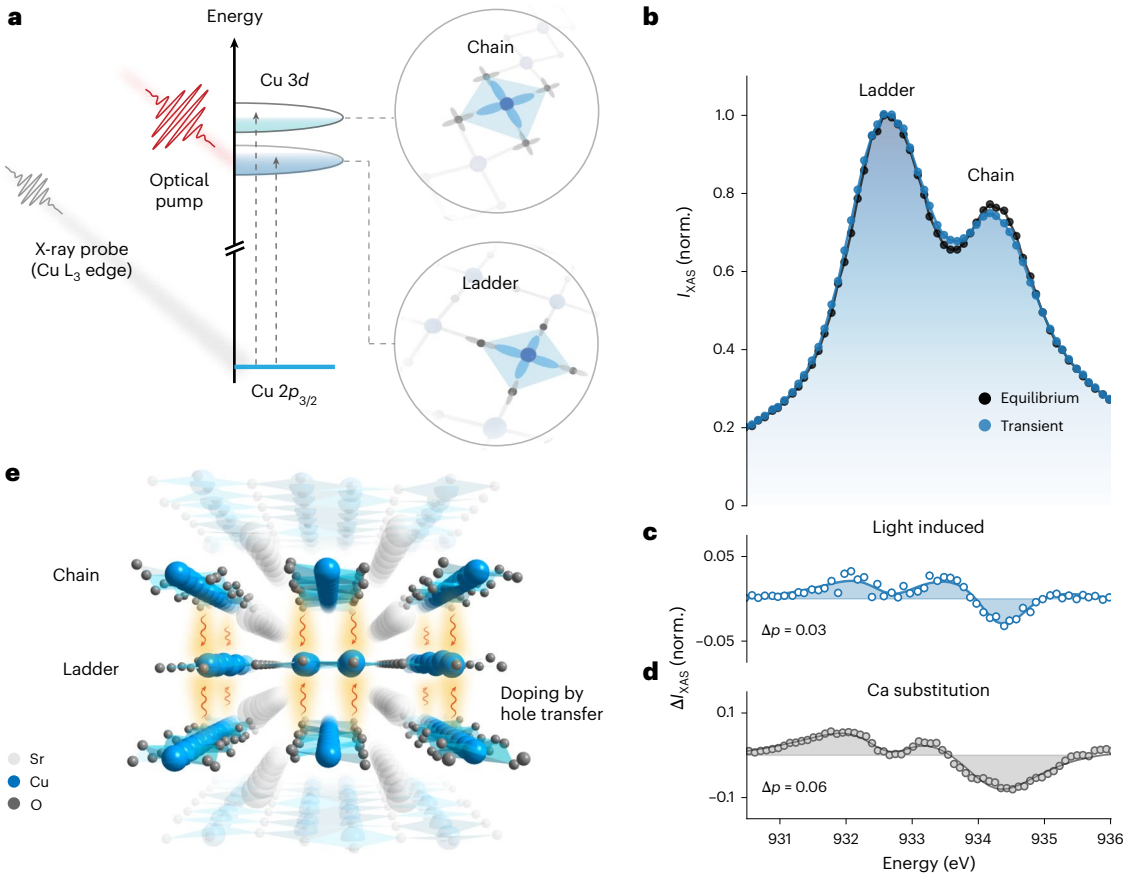

Fig. 4 | Spectroscopic evidence of metastable chain-to-ladder hole transfer. **a**, Schematic of the Cu L_3-edge trXAS experiment. The different chemical environments of the Cu atoms on the corner-sharing ladder and edge-sharing chain result in a double-peaked spectrum. **b**, Equilibrium (black) and transient (blue) Cu L_3-edge XAS at a pump–probe delay of $t = 3$ ps. The two peaks correspond to the ladder (left) and chain (right). **c**, Differential XAS intensity of light-driven $Sr_{14}Cu_{24}O_{41}$ ($I_{XAS}(t = 3\,\text{ps}) - I_{XAS}(t < 0)$). The pump is polarized along the legs with $E_{pump} \approx 7.7$ MV cm^{-1}. **d**, Equilibrium XAS intensity change due to the chain-to-ladder hole transfer induced by Ca substitution in $Sr_{14-x}Ca_xCu_{24}O_{41}$ (ref. 30). We take the difference between the $x = 0$ and $x = 11.5$ compositions, corresponding to a charge transfer of $\Delta p = 0.06$ holes per Cu_L. **e**, Sketch of the pump-induced chain-to-ladder hole transfer. The data are presented as mean values, and the error bars are given by the standard deviation of ten data points measured at negative time delays.

plaquette, where the approximate D_{4h} (point group) symmetry causes hopping contributions from adjacent orbitals to cancel out (Supplementary Section 7).

However, intense in-plane pump electric fields break this symmetry. Optical dressing of the underlying Hamiltonian unbalances hopping contributions from orbitals aligned parallel and perpendicular to the electric field, resulting in a transient, finite t_{ap} (Fig. 6b and Supplementary Section 7). Additionally, the pump introduces a relative energy shift between the ladder Zhang–Rice states and chain apical oxygen orbitals (Supplementary Section 7). The hopping determines the rate of hole transfer between the two subunits, whereas the orbital energy shift dictates the direction and magnitude of hole transfer from the hole-rich ($p_C = 0.50$ holes per Cu_C (Cu_C, Cu atoms in the chain)) chains to the weakly hole-doped ($p_L = 0.06$ holes per Cu_L) ladders[29,30]. This light-activated hopping naturally explains the observed metastability. Although chains and ladders are effectively decoupled at equilibrium, the light-induced enhancement of t_{ap} allows charge transfer between the two subsystems over the duration of the pump pulse. After the pulse coherence dissipates, the chains and ladders decouple again, forming a barrier that protects the light-induced itinerant holes in the ladder from relaxation (Fig. 6c).

This coherent dressing mechanism predicts the light-induced hole transfer from the chains to the ladders to scale as $\Delta p \propto E^2_{pump}$ (Supplementary Fig. 19b). This is consistent with the sign and field dependence of the differential ladder and chain XAS intensities in the metastable state (Supplementary Fig. 9b). The experimentally observed scaling with E^2_{pump} also rules out higher-order dipole-type transitions across the Mott gap, which would instead scale with E^4_{pump}. Finally, contrary to a dipole-type chain-ladder optical transition, such a symmetry-protected charge transfer mechanism would have a vanishing response for an out-of-plane-polarized pump ($E_{pump} \| b$; Supplementary Section 7), in agreement with the experimental polarization dependence of the light-induced charge order suppression (Fig. 3c).

Given that metastability often relies on cooperative structural responses, we finally consider the role of photoinduced lattice changes. One could posit a structural distortion that brings chains and ladders closer and facilitates the transfer of holes between subunits. At equilibrium, hole transfer via Ca substitution indeed coincides with a reduction in both b- and c-axes lattice constants[44]. However, we find no evidence of a major role for structural changes in the metastable state. First, our O K-edge trXAS measurements reveal spectral changes consistent with chain-to-ladder hole transfer, but without the additional blueshift associated with b-axis structural distortions of the ladder O atoms (Supplementary Section 4). Next, since the charge order is commensurate with the ladder unit cell (wavelength, $\lambda = 5c_L$) near $x = 0$ (ref. 45), a contraction of c_L similar to that induced by Ca substitution would shift the charge order scattering momentum q_{CO} by ~2×10^{-3} r.l.u. However, our time-resolved X-ray diffraction (trXRD) measurements show no shift in q_{CO} beyond our fitting uncertainty of ~4×10^{-4} r.l.u., indicating that any changes to c_L in the metastable

https://doi.org/10.1038/s41563-025-02254-2

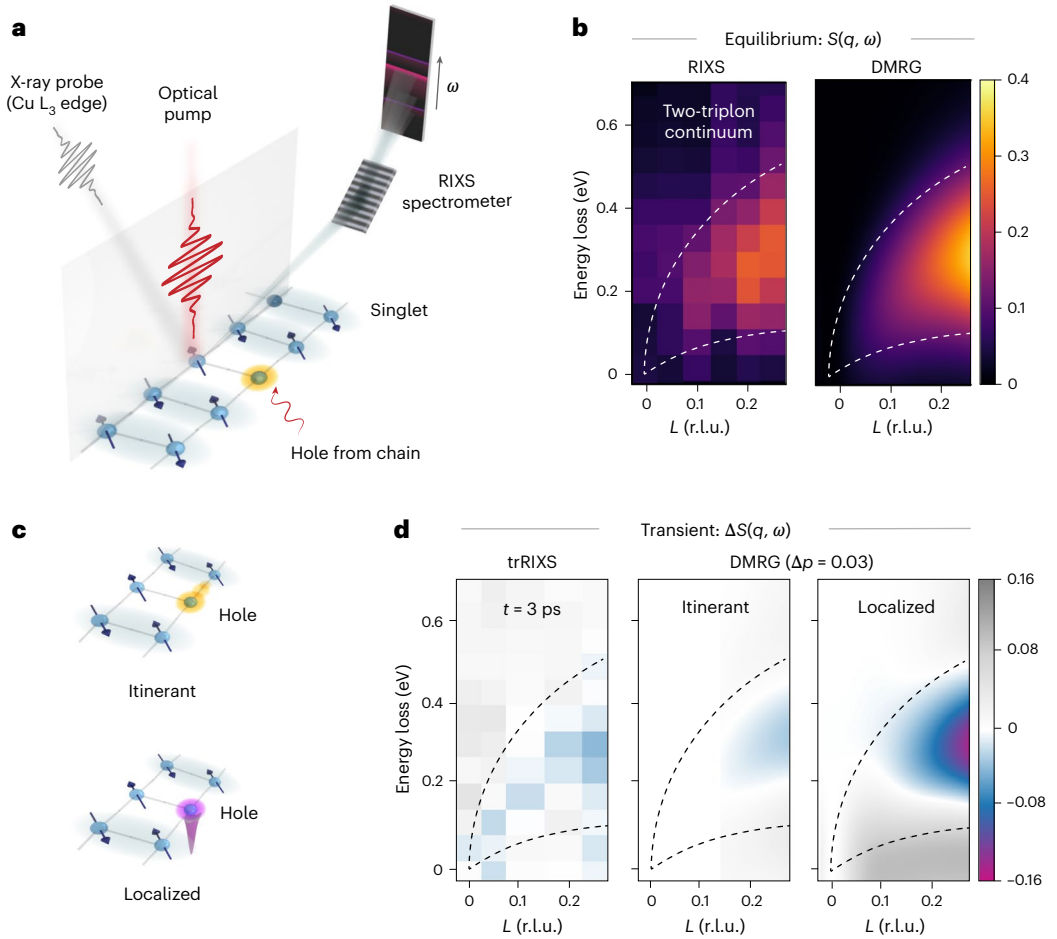

Fig. 5 | Transient magnetic excitation spectrum and onset of electronic metastability. a, Sketch of the Cu L_3-edge trRIXS experiment. The grey clouds denote spin singlets, and the yellow sphere denotes a hole transferred from the chain to the ladder due to pump excitation. **b**, Intensity map of the equilibrium dynamical spin structure factor $S(q, \omega)$ measured by RIXS and calculated using DMRG. The dominant feature is a two-triplon continuum. Its boundaries are indicated by dashed lines as a guide to the eye. **c**, Sketches of itinerant (top) and localized (bottom) holes. **d**, Differential intensity map of the dynamical spin structure factor $S(q, \omega)$ at a pump–probe delay of $t = 3$ ps, as measured by trRIXS (left) and calculated using DMRG for itinerant (centre) and localized (right) quasi-static hole doping of $\Delta p = 0.03$. The trRIXS data are consistent with itinerant hole doping. The RIXS energy resolution is 260 meV.

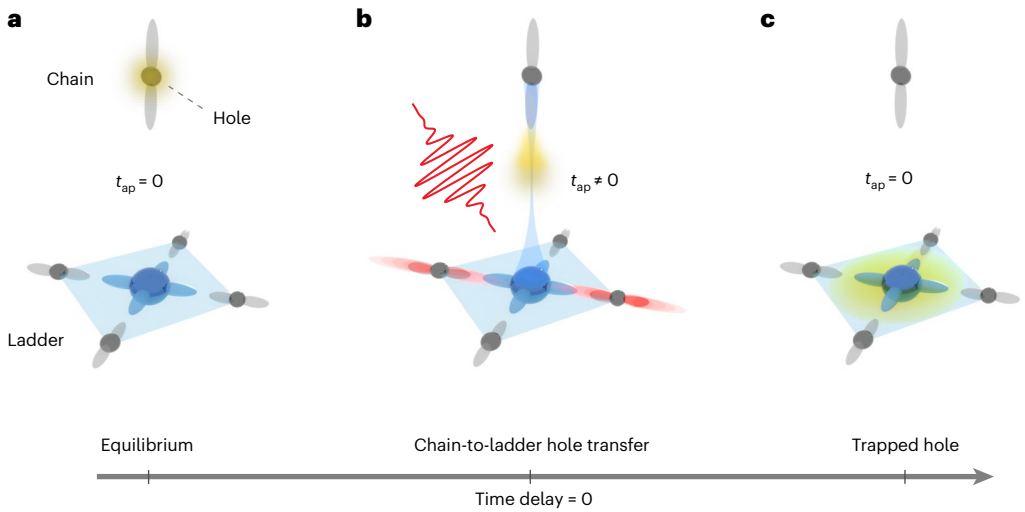

Fig. 6 | Light-induced activation of a symmetry-forbidden tunnelling pathway. a, Each plaquette on the ladder features O 2*p* (grey) and Cu 3*d* (blue) orbitals constituting a Zhang–Rice singlet. At equilibrium, the approximate D_{4h} symmetry of the Zhang–Rice singlet results in vanishing hopping $t_{ap} = 0$ between the CuO_4 plaquette and the apical oxygen. **b**, However, this symmetry is broken when the Hamiltonian is dressed by an intense in-plane pump field E_{pump} (time delay = 0), resulting in a non-zero t_{ap}. The transient activation of the symmetry-forbidden hopping t_{ap} leads to a chain-to-ladder hole transfer. **c**, Once the field is removed, t_{ap} vanishes, trapping the transferred holes in the ladder.

state are much smaller than those accompanying Ca substitution at equilibrium. Finally, the time evolution of our observables, namely, a sudden change upon photoexcitation and the absence of measurable relaxation, contrasts sharply with the typical structural response of other photoexcited cuprates. Their lattice response typically features a picosecond-long saturation build-up[46,47] and a relaxation time well below nanosecond timescales[46,48]. In our experiments, holes are transferred on a resolution-limited timescale (Supplementary Fig. 8), indicating that they are unlikely driven by a structural response of the type observed in other cuprates. Although more subtle structural changes may be resolved with further experimentation, our evidence strongly supports a photoinduced coupling of chains and ladders via apical oxygen hopping as the primary and simplest driver of the observed metastability.

Outlook

Our findings establish Hamiltonian engineering through optical dressing as a powerful strategy to create metastable non-equilibrium states in quantum materials. Although one-dimensional systems are fertile ground for metastability, this approach can be extended to other layered materials such as two-dimensional oxide superconductors[49], hybrid perovskites[50] and van der Waals heterostructures[51]. In these systems, the selective activation of symmetry-forbidden hopping terms could allow for the precise doping of specific bands beyond the limits of chemical substitution, and enable light-driven steering across correlated electronic phases. Additionally, this coherent control protocol could be used to dynamically modulate the interlayer charge distribution in tailored heterostructures for optoelectronic applications at slower timescales. Finally, on cooling, long-lived non-equilibrium charge distributions could give rise to new light-induced phenomena, including spin and orbital ordering, excitonic condensation and η-pairing superconductivity.

Online content

Any methods, additional references, Nature Portfolio reporting summaries, source data, extended data, supplementary information, acknowledgements, peer review information; details of author contributions and competing interests; and statements of data and code availability are available at https://doi.org/10.1038/s41563-025-02254-2.

References

1. Basov, D. N., Averitt, R. D. & Hsieh, D. Towards properties on demand in quantum materials. *Nat. Mater.* **16**, 1077–1088 (2017).
2. Wang, Y. H., Steinberg, H., Jarillo-Herrero, P. & Gedik, N. Observation of Floquet-Bloch States on the surface of a topological insulator. *Science* **342**, 453–457 (2013).
3. McIver, J. W. et al. Light-induced anomalous Hall effect in graphene. *Nat. Phys.* **16**, 38–41 (2020).
4. Shin, D. et al. Phonon-driven spin-Floquet magneto-valleytronics in MoS_2. *Nat. Commun.* **9**, 638 (2018).
5. Disa, A. S. et al. Polarizing an antiferromagnet by optical engineering of the crystal field. *Nat. Phys.* **16**, 937–941 (2020).
6. Fausti, D. et al. Light-induced superconductivity in a stripe-ordered cuprate. *Science* **331**, 189–191 (2011).
7. Mitrano, M. et al. Possible light-induced superconductivity in K_3C_{60} at high temperature. *Nature* **530**, 461–464 (2016).
8. Koshihara, S., Tokura, Y., Mitani, T., Saito, G. & Koda, T. Photoinduced valence instability in the organic molecular compound tetrathiafulvalene-*p*-chloranil (TTF-CA). *Phys. Rev. B* **42**, 6853–6856 (1990).
9. Kiryukhin, V. et al. An X-ray-induced insulator–metal transition in a magnetoresistive manganite. *Nature* **386**, 813–815 (1997).
10. Fiebig, M., Miyano, K., Tomioka, Y. & Tokura, Y. Visualization of the local insulator-metal transition in $Pr_{0.7}Ca_{0.3}MnO_3$. *Science* **280**, 1925–1928 (1998).
11. Zhang, J. et al. Cooperative photoinduced metastable phase control in strained manganite films. *Nat. Mater.* **15**, 956–960 (2016).
12. Stojchevska, L. et al. Ultrafast switching to a stable hidden quantum state in an electronic crystal. *Science* **344**, 177–180 (2014).
13. Stoica, V. et al. Optical creation of a supercrystal with three-dimensional nanoscale periodicity. *Nat. Mater.* **18**, 377–383 (2019).
14. Cremin, K. A. et al. Photoenhanced metastable *c*-axis electrodynamics in stripe-ordered cuprate $La_{1.885}Ba_{0.115}CuO_4$. *Proc. Natl Acad. Sci. USA* **116**, 19875–19879 (2019).
15. Nova, T. F., Disa, A. S., Fechner, M. & Cavalleri, A. Metastable ferroelectricity in optically strained $SrTiO_3$. *Science* **364**, 1075–1079 (2019).
16. Sie, E. J. et al. An ultrafast symmetry switch in a Weyl semimetal. *Nature* **565**, 61–66 (2019).
17. Disa, A. et al. Photo-induced high-temperature ferromagnetism in $YTiO_3$. *Nature* **617**, 73–78 (2023).
18. Budden, M. et al. Evidence for metastable photo-induced superconductivity in K_3C_{60}. *Nat. Phys.* **17**, 611–618 (2021).
19. Vogelgesang, S. et al. Phase ordering of charge density waves traced by ultrafast low-energy electron diffraction. *Nat. Phys.* **14**, 184–190 (2018).
20. Zong, A. et al. Evidence for topological defects in a photoinduced phase transition. *Nat. Phys.* **15**, 27–31 (2019).
21. Gerasimenko, Y. A. et al. Quantum jamming transition to a correlated electron glass in 1T-TaS_2. *Nat. Mater.* **18**, 1078–1083 (2019).
22. von der Linde, D., Glass, A. M. & Rodgers, K. F. Multiphoton photorefractive processes for optical storage in $LiNbO_3$. *Appl. Phys. Lett.* **25**, 155–157 (1974).
23. Zhang, X. et al. Light-induced electronic polarization in antiferromagnetic Cr_2O_3. *Nat. Mater.* **23**, 790–795 (2024).
24. Shan, J.-Y. et al. Giant modulation of optical nonlinearity by Floquet engineering. *Nature* **600**, 235–239 (2021).
25. Sato, S. A. et al. Microscopic theory for the light-induced anomalous Hall effect in graphene. *Phys. Rev. B* **99**, 214302 (2019).
26. Lenarčič, Z., Eckstein, M. & Prelovšek, P. Exciton recombination in one-dimensional organic Mott insulators. *Phys. Rev. B* **92**, 201104 (2015).
27. Mitrano, M. et al. Pressure-dependent relaxation in the photoexcited Mott insulator ET –F_2TCNQ: influence of hopping and correlations on quasiparticle recombination rates. *Phys. Rev. Lett.* **112**, 117801 (2014).
28. Ono, M. et al. Linear and nonlinear optical properties of one-dimensional Mott insulators consisting of Ni-halogen chain and CuO-chain compounds. *Phys. Rev. B* **70**, 085101 (2004).
29. Osafune, T., Motoyama, N., Eisaki, H. & Uchida, S. Optical study of the $Sr_{14-x}Ca_xCu_{24}O_{41}$ system: evidence for hole-doped Cu_2O_3 ladders. *Phys. Rev. Lett.* **78**, 1980 (1997).
30. Nücker, N. et al. Hole distribution in $(Sr,Ca,Y,La)_{14}Cu_{24}O_{41}$ ladder compounds studied by X-ray absorption spectroscopy. *Phys. Rev. B* **62**, 14384 (2000).
31. Abbamonte, P. et al. Crystallization of charge holes in the spin ladder of $Sr_{14}Cu_{24}O_{41}$. *Nature* **431**, 1078–1081 (2004).
32. Vuletić, T. et al. The spin-ladder and spin-chain system $(La,Y,Sr,Ca)_{14}Cu_{24}O_{41}$: electronic phases, charge and spin dynamics. *Phys. Rep.* **428**, 169–258 (2006).
33. Uehara, M. et al. Superconductivity in the ladder material $Sr_{0.4}Ca_{13.6}Cu_{24}O_{41.84}$. *J. Phys. Soc. Jpn* **65**, 2764–2767 (1996).
34. Fukaya, R. et al. Ultrafast electronic state conversion at room temperature utilizing hidden state in cuprate ladder system. *Nat. Commun.* **6**, 8519 (2015).

35. Vuletić, T. et al. Suppression of the charge-density-wave state in $Sr_{14}Cu_{24}O_{41}$ by calcium doping. *Phys. Rev. Lett.* **90**, 257002 (2003).
36. Mitrano, M. et al. Ultrafast time-resolved X-ray scattering reveals diffusive charge order dynamics in $La_{2-x}Ba_xCuO_4$. *Sci. Adv.* **5**, eaax3346 (2019).
37. Huang, M.-J. et al. Determination of hole distribution in $Sr_{14-x}Ca_xCu_{24}O_{41}$ using soft X-ray absorption spectroscopy at the Cu L_3 edge. *Phys. Rev. B* **88**, 014520 (2013).
38. Hammel, P. et al. Localized holes in superconducting lanthanum cuprate. *Phys. Rev. B* **57**, R712 (1998).
39. Tseng, Y. et al. Crossover of high-energy spin fluctuations from collective triplons to localized magnetic excitations in $Sr_{14-x}Ca_xCu_{24}O_{41}$ ladders. *npj Quantum Mater.* **7**, 92 (2022).
40. Dagotto, E., Riera, J. & Scalapino, D. Superconductivity in ladders and coupled planes. *Phys. Rev. B* **45**, 5744 (1992).
41. Schlappa, J. et al. Collective magnetic excitations in the spin ladder $Sr_{14}Cu_{24}O_{41}$ measured using high-resolution resonant inelastic X-ray scattering. *Phys. Rev. Lett.* **103**, 047401 (2009).
42. Kumar, U., Nocera, A., Dagotto, E. & Johnston, S. Theoretical study of the spin and charge dynamics of two-leg ladders as probed by resonant inelastic X-ray scattering. *Phys. Rev. B* **99**, 205130 (2019).
43. Gotoh, Y. et al. Structural modulation, hole distribution, and hole-ordered structure of the incommensurate composite crystal $(Sr_2Cu_2O_3)_{0.70}CuO_2$. *Phys. Rev. B* **68**, 224108 (2003).
44. Deng, G. et al. Structural evolution of one-dimensional spin-ladder compounds $Sr_{14-x}Ca_xCu_{24}O_{41}$ with Ca doping and related evidence of hole redistribution. *Phys. Rev. B* **84**, 144111 (2011).
45. Rusydi, A. et al. Quantum melting of the hole crystal in the spin ladder of $Sr_{14-x}Ca_xCu_{24}O_{41}$. *Phys. Rev. Lett.* **97**, 016403 (2006).
46. Gedik, N., Yang, D.-S., Logvenov, G., Bozovic, I. & Zewail, A. H. Nonequilibrium phase transitions in cuprates observed by ultrafast electron crystallography. *Science* **316**, 425–429 (2007).
47. Mansart, B. et al. Temperature-dependent electron-phonon coupling in $La_{2-x}Sr_xCuO_4$ probed by femtosecond X-ray diffraction. *Phys. Rev. B* **88**, 054507 (2013).
48. Mankowsky, R. et al. Nonlinear lattice dynamics as a basis for enhanced superconductivity in $YBa_2Cu_3O_{6.5}$. *Nature* **516**, 71–73 (2014).
49. Keimer, B., Kivelson, S. A., Norman, M. R., Uchida, S. & Zaanen, J. From quantum matter to high-temperature superconductivity in copper oxides. *Nature* **518**, 179–186 (2015).
50. Shi, R., Long, R., Fang, W.-H. & Prezhdo, O. V. Rapid interlayer charge separation and extended carrier lifetimes due to spontaneous symmetry breaking in organic and mixed organic–inorganic Dion–Jacobson perovskites. *J. Am. Chem. Soc.* **145**, 5297–5309 (2023).
51. Jin, C. et al. Ultrafast dynamics in van der Waals heterostructures. *Nat. Nanotechnol.* **13**, 994–1003 (2018).

[1]Department of Physics, Harvard University, Cambridge, MA, USA. [2]Department of Applied Physics, Harvard University, Cambridge, MA, USA. [3]Department of Chemistry, Emory University, Atlanta, GA, USA. [4]Department of Physics, The Chinese University of Hong Kong, Hong Kong, China. [5]Diamond Light Source, Didcot, UK. [6]National Synchrotron Light Source II, Brookhaven National Laboratory, Upton, NY, USA. [7]PSI Center for Photon Science, Paul Scherrer Institute, Villigen, Switzerland. [8]Department of Physics, Pohang University of Science and Technology, Pohang, Korea. [9]Max Planck POSTECH/Korea Research Initiative, Center for Complex Phase Materials, Pohang, Korea. [10]Condensed Matter Physics and Materials Science Department, Brookhaven National Laboratory, Upton, NY, USA. [11]Department of Physics, Pennsylvania State University, University Park, PA, USA. [12]2D Crystal Consortium, Materials Research Institute, Pennsylvania State University, University Park, PA, USA. [13]Pohang Accelerator Laboratory (PAL), Pohang University of Science and Technology, Pohang, South Korea. [14]Department of Physics, University of Trento, Povo, Italy. ✉e-mail: hpadmanabhan@g.harvard.edu; yao.wang@emory.edu; mmitrano@g.harvard.edu

Methods

Crystal synthesis and characterization

High-quality single crystals of $Sr_{14}Cu_{24}O_{41}$ were grown using a modified travelling solvent floating zone technique. We started by synthesizing polycrystalline $Sr_{14}Cu_{24}O_{41}$ via a solid-state reaction and, subsequently, used it as a feed material rod. Choosing CuO as the flux, we prepared the flux rod (seed) for the travelling solvent floating zone growth by mixing $Sr_{14}Cu_{24}O_{41}$ and CuO powders with a mass ratio of $Sr_{14}Cu_{24}O_{41}$:CuO = 1:0.0163. To ensure stable growth, we tuned the feed speed of the feed rod within 0.81–2.2 mm h^{-1}, and set the growth speed to 0.81 mm h^{-1}. We rotated both rods in mutually opposite directions at 30 rpm and finally obtained a crystalline rod (2 cm in length and 4 mm in diameter). We confirmed the crystal quality and lattice structure via X-ray diffraction measurements, finding good agreement with previous reports[52]. The crystal lattice parameters are $a = 11.47$ Å, $b = 13.35$ Å and $c = 7c_L = 10c_C = 27.46$ Å, where the L and C subscripts indicate ladder and chain subunits, respectively.

Time-resolved time-domain THz spectroscopy measurements

The optical setup for our time-resolved time-domain THz spectroscopy experiments was seeded by a Ti:sapphire regenerative amplifier (800-nm wavelength, 35-fs pulse duration, 2-kHz repetition rate). We split the beam into three branches. The first branch (0.25-mJ pulse energy) was used for the pump excitation. The second branch (0.5-mJ pulse energy) was used to generate quasi-single-cycle THz probe pulses with spectral components between 1 THz and 5 THz (4–20 meV) via optical rectification in a 0.2-mm-thick ⟨110⟩ GaP crystal. The third branch (0.05-mJ pulse energy) was used as an optical gate for the electro-optic sampling (EOS) of the probe pulses reflected from the sample surface. The pump delay was controlled by a mechanical delay stage on the pump beam.

Single-shot THz detection. We used echelon-based single-shot detection[53] to measure equilibrium and transient THz fields. The optical gate pulse was routed through an echelon mirror, resulting in a temporally offset array (spacing, 20 fs) of pulselets spanning a 10-ps time window. We focused the pulselets onto a 0.2-mm-thick ⟨110⟩ GaP crystal to perform single-shot EOS of the probe pulses reflected from the sample surface. The transmitted beam was split into perpendicularly polarized components using a quarter-wave plate and a Wollaston prism, and each component was imaged on a linear array detector (Synertronics Glaz LineScan with a Hamamatsu S11637-2048Q sensor). The final THz waveform was obtained by calibrating and subtracting the two images, resulting in $E(t_{EOS})$, where t_{EOS} is the THz EOS time delay. For our pump–probe experiments, we measured this as a function of the pump delay t to obtain a two-dimensional map $E(t_{EOS}, t)$. We interpolated and appropriately translated the measured $E(t_{EOS}, t)$ along the t axis to ensure that the transient waveform at each t was measured with the gate and pump pulses at the same t_{EOS} (ref. 54).

Time-resolved time-domain THz spectroscopy measurements. We conducted our measurements in a reflection geometry on freshly cleaved a–c surfaces of $Sr_{14}Cu_{24}O_{41}$ single crystals. The THz probe beam was s polarized ($E \| c$) and focused onto the sample at an angle of incidence of 60°, using an off-axis parabolic mirror. The reflected light was focused onto the GaP crystal for the EOS. The pump beam was focused onto the sample at normal incidence with a spot size of 1,400 µm, whereas the probe spot size was 600 µm. We mechanically chopped the pump at twice the repetition rate of the probe beam. The linear array detectors were connected to a digitizer synchronized to the mechanical choppers, which sorted the detected THz waveforms into 'pump on' and 'pump off' conditions. This allowed us to simultaneously acquire the equilibrium and transient THz waveforms, and eliminate any possible artifacts due to long-term drift and residual pump scattering.

Reconstruction of transient optical conductivity. The equilibrium electric field $E_0(t_{EOS})$ and differential transient electric field $\Delta E(t_{EOS}, t)$ were independently Fourier transformed to obtain the complex Fresnel reflection coefficient $\tilde{r}(\omega, t)$ using the expression

$$\Delta\tilde{E}/\tilde{E}_0 = (\tilde{r}(\omega, t) - \tilde{r}_0(\omega))/\tilde{r}_0(\omega), \quad (1)$$

where $\tilde{r}_0$ is the reflection coefficient calculated from the equilibrium optical response (Supplementary Section 1 and Supplementary Fig. 1). From this, we evaluated the transient refractive index $\tilde{n}(\omega, t)$. Since the probe penetration depth (45–50 µm) is a factor of 150 larger than that of the pump (0.32 µm), we used the thin-film approximation, where it is assumed that a thin layer at the sample surface is homogeneously photoexcited, whereas the bulk remains unperturbed[6,55]. The analytical expression for the transient change to the optical conductivity in the photoexcited volume is given by

$$\Delta\tilde{\sigma}(\omega, t) = \left(\frac{1}{377 \times \delta}\right) \frac{\frac{\Delta\tilde{E}(\omega,t)}{\tilde{E}_0(\omega)}\left(\tilde{n}^2(\omega, t) - 1\right)}{\frac{\Delta\tilde{E}(\omega,t)}{\tilde{E}_0(\omega)}\left[\cos\theta_0 - \sqrt{\tilde{n}^2(\omega, t) - \sin^2\theta_0}\right] + 2\cos\theta_0}, \quad (2)$$

where δ is the pump penetration depth and θ_0 is the probe angle of incidence.

trXAS and trRIXS measurements

We conducted trXAS and trRIXS measurements at the Furka endstation[56] of the Athos beamline at SwissFel, Paul Scherrer Institut[57]. The repetition rate was 100 Hz. The X-ray beam was horizontally polarized and focused to a spot size of 600 µm (H) × 10 µm (V). Shot-to-shot X-ray intensity fluctuations were recorded with an avalanche photodiode (APD) and used to normalize the signals. We used 800-nm (1.55-eV), 100-fs-long pump pulses, which were focused down to a diameter of 1,300 µm to achieve fluences up to 8 mJ cm^{-2} (approximately 8 MV cm^{-1}). The pump penetration depth (0.32 µm) exceeded that of the soft X-ray probe at the Cu L_3 edge (~0.2–0.3 µm) at all the measured angles of incidence, thereby resulting in a homogeneously excited probed sample volume. We cleaved the sample along the b axis in situ, and mounted it with the b–c axes in the scattering plane. The temperature was fixed to 100 K for all the measurements.

trXAS measurements. We acquired the spectra in the fluorescence-yield mode at the Cu L_3 edge, with the X-ray beam near normal incidence and detected by an avalanche photodiode at $2\theta = 78°$. We acquired 2,000 pulses at each time delay for the time-dependent XAS intensity traces and 1,000 pulses at each monochromator energy for the trXAS spectra.

trRIXS measurements. We acquired the RIXS spectra using incident X-rays resonant with the Cu L_3 peak at 932.6 eV. Our measurements were performed with the scattering angle 2θ fixed at 130° and the incident angle θ varied from 65° to 93°, corresponding to momentum transfers from $L = 0$ to $L = 0.25$ r.l.u. (defined in units of $2\pi/c_L$). Given the low-dimensional nature of the spin fluctuations, we neglected dispersion along the K direction. The RIXS spectrometer had a combined energy resolution of 260 meV. We collected the trRIXS spectra by acquiring 30,000 shots each with the pump laser on and off, and averaging over 8 scans each, measured in an alternating manner to monitor and eliminate artefacts due to slow drifts. To avoid possible sample damage due to sustained exposure to the intense X-ray FEL beam, we shifted the sample position by 200 µm on the completion of a dataset. We note that this is a standard protocol used for trRIXS measurements due to the relatively long acquisition times. The raw spectra, subtraction of the elastic line and extraction of the dynamical spin structure factor $S(q, \omega)$ are shown in Supplementary Section 5 and Supplementary Figs. 10–13.

trXRD measurements

We conducted the trXRD resonant measurements with the O K edge at 528.6 eV at the RSXS endstation of the Pohang Accelerator Laboratory X-ray Free Electron Laser running at a repetition rate of 30 Hz. The X-ray pulses were horizontally polarized and focused to a spot size of 160 μm (H) × 295 μm (V). We recorded shot-to-shot intensity fluctuations using a gas monitor detector and used them to normalize the signals. The pump pulses had a duration of 100 fs, and were focused to a spot size of 585 μm (H) × 549 μm (V), with fluences up to 6 mJ cm^{-2}. The pump penetration depth (0.32 μm) is comparable with that of the O K-edge X-ray probe (0.28 μm). Measurements were done on a polished sample, with the surface normal oriented parallel to the c axis with a miscut of 10°. We detected the charge order peak using an APD at $q = [0, 0, 0.2]$ by fixing θ at 36° and 2θ at 72°. The momentum dependence was mapped via a θ–2θ scan. The APD had a 3-mm aperture, and was located 90 mm from the sample. Details about the subtraction of the fluorescent background are provided in the Supplementary information. We additionally conducted the O K-edge trXAS measurements, outlined in Supplementary Section 4. We acquired the spectra in the fluorescence-yield mode, with the X-ray beam near normal incidence and detected by an APD at $2\theta = 110°$. All the measurements were performed at 100 K.

DMRG calculations

We used DMRG to calculate the ground state $|G\rangle$ of an extended Hubbard model, described by the Hamiltonian

$$\begin{aligned}\mathcal{H} = &-\sum_{jl\sigma} t\left[c^{(l)\dagger}_{j\sigma}c^{(l)}_{j+1\sigma} + \text{h.c.}\right] - \sum_{j\sigma} t_\perp\left[c^{(0)\dagger}_{j\sigma}c^{(1)}_{j\sigma} + \text{h.c.}\right]\\ &-\sum_{jl\sigma} t'\left[c^{(l)\dagger}_{j\sigma}c^{(1-l)}_{j+1\sigma} + \text{h.c.}\right] + U\sum_{jl} n^{(l)}_{j\uparrow}n^{(l)}_{j\downarrow}\\ &+V\sum_j\sum_{\sigma,\sigma'}\left[n^{(0)}_{j\sigma}n^{(1)}_{j\sigma'} + \sum_l n^{(l)}_{j\sigma}n^{(l)}_{j+1\sigma'}\right],\end{aligned} \tag{3}$$

where $c^{(l)}_{j\sigma}$ ($c^{(l)\dagger}_{j\sigma}$) annihilates (creates) an electron at site j on leg $l = 0, 1$ with spin $\sigma = \uparrow, \downarrow$, and $n^{(l)}_{j\sigma} = c^{(l)^\dagger}_{j\sigma}c^{(l)}_{j\sigma}$ denotes the local electron density. We take the on-site Coulomb interaction $U = 8t$, $t_\perp = 0.84t$, $t' = -0.3t$ and an attractive nearest-neighbour interaction $V = -1.25t$[58]. We use the time-dependent variational principle to simulate the time evolution of the wavefunction after a local spin excitation[59], giving an unequal-time correlation function

$$S(q,\omega) = \int_0^{T_{\max}} \mathrm{d}t \sum_j \sum_{l=0,1} \left\langle G\middle|\mathcal{U}(0,t)S^{(l)}_j\mathcal{U}(t,0)S^{(0)}_{j_0}\middle|G\right\rangle \mathrm{e}^{\mathrm{i}qj}\mathrm{e}^{-\mathrm{i}\omega t}, \tag{4}$$

which corresponds to the RIXS measurements with matrix-element corrections applied. Here $S^{(l)}_j = \left[c^{(l)\dagger}_{j\uparrow}c^{(l)}_{j\uparrow} - c^{(l)\dagger}_{j\downarrow}c^{(l)}_{j\downarrow}\right]/2$ is the spin operator at site j on leg l, and $\mathcal{U}(t_1, t_2)$ is the time evolution operator. To minimize the boundary effects and enforce translational symmetry, the middle site $j_0 = L/2$ is fixed, and the sum in equation (4) runs over all the site indices j. In this work, we keep the maximum bond dimension $D = 1{,}000$, with truncation error around 10^{-7}. The time evolution has a step $\delta t = 0.05t^{-1}$ and is truncated at $T_{\max} = 30t^{-1}$. All the DMRG results are obtained using a two-leg ladder with $L_x = 64$ and broadened to match the experimental energy resolution.

Density functional theory calculations

Density functional theory (DFT) simulations of the electronic structure and the Cu L_3-edge XAS spectra have been carried out using QUANTUM ESPRESSO v. 7.3.1 (refs. 60,61) via the PW.X and XSPECTRA.X packages[62–65]. QUANTUM ESPRESSO implements DFT within the pseudopotential and plane-wave approaches. For our simulations, we used ultrasoft pseudopotentials with gauge-invariant projector augmented wave reconstructions[66], nonlinear core corrections and two projectors per angular momentum channel to ensure the convergence of the XAS spectra. We imposed a kinetic energy cut-off of 50 Ry (680 eV) on the plane-wave basis set for the Kohn–Sham wavefunctions and 500 Ry (6,800 eV) for the electronic density. Electron exchange–correlation effects have been treated using the Perdew–Burke–Ernzerhof generalized gradient approximation[67] with Hubbard + U corrections applied to the Cu d (10.0 eV) and O p (4.0 eV) states[68]. We adopted the rotationally invariant DFT + U approach using orthogonalized atomic orbitals as the Hubbard projectors[69]. For the DFT steps, the integration of the first Brillouin zone has been conducted using a 2 × 2 × 1 regular Γ-centred **k**-point mesh. For the calculation of the XAS spectrum, the **k**-point mesh is shifted by half a grid spacing along each of the Cartesian directions.

These simulation parameters and the initial atomic coordinates and magnetic ordering of the 1 × 1 × 4 supercell have been adapted from a previous investigation of the O K edge in the same compound[68]. The stoichiometry of the system investigated was $Cu_{96}O_{164}Sr_{56}$ and the dimensions of the supercell were $a = b = 8.825$ Å, $c = 55.058$ Å and angle $\angle ab = 81.146°$. The crystal structure has been relaxed (using atomic orbitals as Hubbard projectors) with the Broyden–Fletcher–Goldfarb–Shanno quasi-Newton algorithm; once a force tolerance of 1.3×10^{-3} atomic units was reached, the structure was deemed to be relaxed. For the calculation of the Cu L_3-edge XAS spectrum, we created isolated ladder ($Cu_{56}O_{84}$) and chain ($Cu_{40}O_{80}$) subunits maintaining the same supercell dimensions as the parent compound. Treating the subunits in isolation enabled us to simulate the effects of charge transfer by modulating the number of holes on each component. We applied a total charge of +4.0e and +20.0e on the ladder and chain, respectively, which corresponds to the equilibrium state. For the optically pumped state, to simulate hole transfer, these charges were set to +6.0e and +18.0e for the ladder and chain, respectively. These charges have been chosen to match with the experimentally determined ladder hole densities of 0.06 per Cu_L and 0.09 per Cu_L. The XAS spectra were computed at each inequivalent Cu site within the dipole approximation, along the [0 0 1] polarization direction using the Lanczos–Haydock recursive fraction algorithm[62]. A Lorentzian broadening of 300 meV is applied to the final spectrum to account for core-hole broadening effects.

Data availability

The data that support the findings of this study are present in the article and its Supplementary Information. Source data for figures in the main text are available via Figshare at https://doi.org/10.6084/m9.figshare.28851200.v1. Any additional data are available from the corresponding authors upon request.

Code availability

The codes used for DMRG and CuO6 cluster calculations are available from the corresponding authors upon request.

References

52. Vanishri, S. et al. Crystal growth and characterization of two-leg spin ladder compounds: $Sr_{14}Cu_{24}O_{41}$ and $Sr_2Ca_{12}Cu_{24}O_{41}$. *J. Cryst. Growth* **311**, 3830–3834 (2009).
53. Gao, F. Y., Zhang, Z., Liu, Z.-J. & Nelson, K. A. High-speed two-dimensional terahertz spectroscopy with echelon-based shot-to-shot balanced detection. *Opt. Lett.* **47**, 3479–3482 (2022).
54. Hu, W. et al. Optically enhanced coherent transport in $YBa_2Cu_3O_{6.5}$ by ultrafast redistribution of interlayer coupling. *Nat. Mater.* **13**, 705–711 (2014).
55. Hunt, C. R. *Manipulating Superconductivity in Cuprates with Selective Ultrafast Excitation*. PhD thesis, Univ. of Illinois at Urbana-Champaign (2015).
56. SwissFEL Furka (2025); https://www.psi.ch/en/swissfel/furka
57. Abela, R. et al. The SwissFEL soft X-ray free-electron laser beamline: Athos. *J. Synchrotron Rad.* **26**, 1073–1084 (2019).

58. Padma, H. et al. Beyond-Hubbard pairing in a cuprate ladder. *Phys. Rev. X* **15**, 021049 (2025).
59. Haegeman, J. et al. Time-dependent variational principle for quantum lattices. *Phys. Rev. Lett.* **107**, 070601 (2011).
60. Giannozzi, P. et al. QUANTUM ESPRESSO: a modular and open-source software project for quantum simulations of materials. *J. Phys.: Condens. Matter* **21**, 395502 (2009).
61. Giannozzi, P. et al. Advanced capabilities for materials modelling with Quantum ESPRESSO. *J. Phys.: Condens. Matter* **29**, 465901 (2017).
62. Taillefumier, M., Cabaret, D., Flank, A.-M. & Mauri, F. X-ray absorption near-edge structure calculations with the pseudopotentials: application to the K edge in diamond and α-quartz. *Phys. Rev. B* **66**, 195107 (2002).
63. Gougoussis, C., Calandra, M., Seitsonen, A. P. & Mauri, F. First-principles calculations of X-ray absorption in a scheme based on ultrasoft pseudopotentials: from α-quartz to high-T_C compounds. *Phys. Rev. B* **80**, 075102 (2009).
64. Gougoussis, C. et al. Intrinsic charge transfer gap in NiO from Ni K-edge X-ray absorption spectroscopy. *Phys. Rev. B* **79**, 045118 (2009).
65. Bunau, O. & Calandra, M. Projector augmented wave calculation of X-ray absorption spectra at the $L_{2,3}$ edges. *Phys. Rev. B* **87**, 205105 (2013).
66. Pickard, C. J. & Mauri, F. All-electron magnetic response with pseudopotentials: NMR chemical shifts. *Phys. Rev. B* **63**, 245101 (2001).
67. Perdew, J. P., Burke, K. & Ernzerhof, M. Generalized gradient approximation made simple. *Phys. Rev. Lett.* **77**, 3865–3868 (1996).
68. Ilakovac, V. et al. Hole depletion of ladders in $Sr_{14}Cu_{24}O_{41}$ induced by correlation effects. *Phys. Rev. B* **85**, 075108 (2012).
69. Dudarev, S. L., Botton, G. A., Savrasov, S. Y., Humphreys, C. J. & Sutton, A. P. Electron-energy-loss spectra and the structural stability of nickel oxide: an LSDA+*U* study. *Phys. Rev. B* **57**, 1505–1509 (1998).

Acknowledgements

We thank C. Bernhard, A. Cavalleri, S. Chattopadhyay, R. Comin, E. Demler, M. Eckstein, T. Giamarchi, V. Ilakovac and S. Johnston for insightful discussions. Experimental part of this work was primarily supported by the US Department of Energy, Office of Basic Energy Sciences, Early Career Award Program, under award no. DE-SC0022883. Theoretical part of the work (L.X., Z.S. and Yao Wang) was supported by the Air Force Office of Scientific Research Young Investigator Program under grant no. FA9550-23-1-0153. Work performed at Brookhaven National Laboratory was supported by the US Department of Energy, Division of Materials Science, under contract no. DE-SC0012704. B. Lee and H.J. were supported by the National Research Foundation of Korea (MSIT), grant nos. 2022M3H4A1A04074153 and 2020M3H4A2084417. M.C. acknowledges support from the European Union (ERC, DELIGHT, 101052708). We acknowledge the Paul Scherrer Institut, Villigen, Switzerland, for the provision of beamtime at the Furka beamline of the SwissFEL. The work at PAL-XFEL was performed at the RSXS endstation (proposal no. 2023-1st-SSS-002), funded by the Korean government (MSIT). The single-crystal growth work was performed at the Pennsylvania State University Two-Dimensional Crystal Consortium—Materials Innovation Platform (2DCC-MIP), which is supported by NSF Cooperative Agreement no. DMR-2039351. J.D.E. and M.C. are supported by The Royal Society, grant no. IES/R3/223185. We acknowledge computational resources from ARCHER2 UK National Computing Service, which was granted via HPC-CONEXS, the UK High-End Computing Consortium (EPSRC grant no. EP/X035514/1). The simulation used resources of the Frontera computing system at the Texas Advanced Computing Center.

Author contributions

H.P. and M.M. conceived the project. M.M. supervised the project. H.P. and F.G. conducted the time-resolved time-domain THz spectroscopy measurements. C.C.H. performed the equilibrium optical spectroscopy measurements. H.P., S.F.R.T., M.P.M.D., M.M., E.S., H.U., B. Liu, E.P., A.R. and E.R. conducted the Cu L_3-edge trXAS and trRIXS measurements. H.P., S.F.R.T., B. Lee, H.C., S.-Y.P. and H.J. conducted the O K-edge trXAS and trXRD measurements. Yu Wang, S.H.L. and Z.M. synthesized the samples. H.P., W.H. and S.F.R.T. prepared and precharacterized the samples. Yao Wang developed the theoretical model for the light-activated hopping mechanism. Z.S. and H.W. performed the DMRG calculations and L.X. performed the ab initio simulations under the supervision of Yao Wang. J.D.E. and M.C. performed the DFT calculations. H.P. analysed the data. H.P., Yao Wang and M.M. wrote the paper with input from all authors.

Competing interests

The authors declare no competing interests.

Additional information

Supplementary information The online version contains supplementary material available at https://doi.org/10.1038/s41563-025-02254-2.

Correspondence and requests for materials should be addressed to Hari Padma, Yao Wang or Matteo Mitrano.

Peer review information *Nature Materials* thanks Dragan Mihailovic and the other, anonymous, reviewer(s) for their contribution to the peer review of this work.